Observations of seismoacoustic *T* waves at and beneath the sea floor in the deep ocean

Rhett Butler

The IRIS Consortium, 1200 New York Avenue NW, Washington DC 20005

and

University of Hawaii at Manoa, 1680 East West Road, Honolulu, HI 96822

Submitted to J. Acoust Soc. Am.

Abstract.

The combined use of seismic and hydrophone observations show that the traditional *T* wave propagates as a seismoacoustic, interface wave (*Ti*) coupled to the seafloor. Seismoacoustic *Ti* waves propagating at the sound speed of water are routinely observed over megameter distances at the deep (4979 m) seafloor Hawaii-2 Observatory (H2O) between Hawaii and California, even though the seafloor site is within a shadow zone for acoustic wave propagation. *Ti* has also been observed 225 km SSW of Oahu at the OSN1 site at the seafloor and within its ODP borehole into the basalt basement. Analyses of timing, apparent velocity, energy, and polarization of these interface waves are presented. At low frequency (< ~5 Hz) *Ti* propagates dominantly in the sediments and is consistent with coupled higher-mode Rayleigh waves. At higher frequencies the observed *Ti* waves show characteristics consistent with acoustic scattering. Although no single scattering mechanism appears to be capable of generating the observed *Ti* waves, internal waves, spiciness, acoustic bio-scattering, and sea surface roughness may contribute to the observations. The observation of *Ti* from an earthquake in Guatemala at OSN1, whose path is blocked by the Island of Hawaii, suggests scattering from the vicinity of the Cross Seamount.

PACS numbers: 4330-k, 4330Qd, 4335Pt

I. Introduction

T waves are generated by earthquakes occurring beneath the seafloor, and propagate acoustically for great distances in the ocean. They are routinely used for monitoring oceanic earthquake locations (*e.g.,* Fox et al., 2001), and for nuclear Treaty monitoring using a combination of hydrophone arrays and seismic stations on islands (*e.g.,* Okal*,* 2001). Although the Hawaii-2 Observatory (H2O) (Butler *et al.*, 2000; Butler *et al.,* 2004) between Hawaii and California at 4979 m depth lies nearly a kilometer below the conjugate depth of the SOFAR channel, interface *T* waves (*Ti*) are observed (Figure 1) from circum-Pacific earthquakes at thousands of kilometers propagating as coupled higher mode Rayleigh waves at the seismoacoustic boundary at the seafloor (Butler and Lomnitz, 2002). *Ti* waves are energetically observed at the H2O site regardless of season or propagation azimuth. Although *Ti* waves at H2O typically have frequencies up to about 35 Hz, energy up to 80 Hz has been observed.

In the Acoustic Thermometry of Ocean Climate experiment (ATOC), acoustic sources (75 Hz) and receivers located within the SOFAR channel are also used to monitor ocean temperature change integrated over great distances via the associated travel time variation of sound with temperature. However, even in these controlled experiments, sound arrivals are observed at megameter distances on hydrophones in the shadow zone below the conjugate depth (some of these observations are near H2O) that remain unexplained (Dushaw et al., 1999).

Seismoacoustic *Ti* has also been observed at the OSN1 site 225 km SSW of Oahu, on a seismometer buried in the sediments at the seafloor 4400 m depth and in a borehole seismometer emplaced below the sediment-basalt interface 242.5 m below the seafloor,

from earthquakes 300 km distant in Hawaii and 7270 km distant near Guatemala (Butler, 2001). Although the observation of *Ti* waves in a borehole deep beneath the seafloor is remarkable enough, the propagation path from the Guatemala earthquake to OSN1 is blocked by the Island of Hawaii.

The observational study presented in this paper uses apparent velocity, seismoacoustic energy partitioning, and polarization analyses of H2O data to characterize *Ti* wave observations at the seafloor below the conjugate depth. The *Ti* waves show both characteristics of seismoacoustically coupled interface waves as well as acoustic scattering interactions from the upper ocean. Polarization and time analysis suggests that the *Ti* waves observed seismically in the ODP borehole at OSN1 propagate as evanescent interface waves. Scattering of *T* waves by seamounts to the seafloor is indicated from the vicinity of the Cross Seamount southwest of Hawaii.

II. Observations

A. H2O

The sound speed at the axis of the SOFAR channel is about 1.48 km/s, whereas at the seafloor at H2O the speed is about 1.54 km/s (Levitus *et al.,* 1994; Levitus and Boyer, 1994; Dushaw, 1999). Oceanic earthquakes often lack local epicentral control and the trade-offs between origin time, depth, and location create large uncertainty in estimating apparent velocity of *T* waves to this precision. However, since this velocity uncertainty decreases with distance, the most distant earthquakes can be used to discriminate the apparent velocity (Figure 2). The *Ti* waves from events over 5000 km northwest of H2O and over 9000 km south of H2O arrive with apparent velocities of about 1.48 to 1.49 km/s.

Acoustic wave propagation modeling of the most distant event using a standard Pacific ocean acoustic and bathymetric model predicts arrivals in the SOFAR channel at these corresponding arrival times, but not at the depth of H2O (Dushaw, personal communication, 2002). This circumstantial evidence indicates that the *Ti* arrivals at H2O travel in or coupled with the SOFAR channel.

The seismoacoustic *Ti* wave arrivals are recorded on the both a seismometer, buried about 0.5 m in the seafloor, and on a hydrophone located about 0.5 m above the seafloor. The partitioning of energy above and below the seafloor interface is diagnostic of the propagation mode of the *Ti* waves (Figure 3). The horizontal components of seismic motion are rotated into radial and transverse direction with respect to the great circle from the source. The seismoacoustic modal structure observed by Butler and Lomnitz (2002) is clearly evident. Both for these two distant events and for closer events analyzed, the energy on the hydrophone channel is greater than the sum of the seismic channels at frequencies above about 5 Hz. Below 5 Hz, the energy on the radial component of the seismometer dominates, except for the most distant event at 9400 km (where no substantial arrival is observed at low frequency above the normal background noise). Strong polarization is characteristic of *Ti* waves at frequencies ~5 Hz observed at H2O (Figure 4) with dominant motion radially from the source and 2° downward. Thus, whereas below about 5 Hz, the energy of the *Ti* wave is dominantly in the seafloor, above 5 Hz there is a more energy propagating acoustically in the water. Since the sound speed of water near the seafloor of the H2O site is much greater (1.54 km/s), the dominance of acoustic energy above 5 Hz traveling with an apparent velocity at 1.48-1.49 km/s suggests that this energy is being

scattered from the SOFAR channel to the seafloor, where it locally couples to seismoacoustic modes.

Without benefit from a spatial array of sensors, a single hydrophone provides no information on the directionality of a propagating wave. However, the seismometer provides indirect indication of the directionality of acoustic particle velocity through the polarization of the coupled seismic wave field. By examining the seismic polarization of specific seismoacoustic modes (Figure 5), we can infer properties of the acoustic propagation. The propagation of low-frequency (<5 Hz) *Ti* waves as higher-order Rayleigh waves is clearly indicated by the prograde and retrograde elliptical particle motion in the sagittal plane (radial-vertical). The mode propagates at an angle of about 2º from horizontal (down and away from the source), and within 4º of azimuth of the great circle axis. At higher frequencies the seismoacoustic modes display a wider range of polarization characteristics. At times some of the modes (Figure 5) show a nearly rectilinear pattern characteristic of a body wave being scattered from above at large angles (>30º from the horizontal). Other modes sometimes display elliptical motion along an axis at greater angle to the horizontal (5º to 45º) than exhibited by the low-frequency modes that propagate dominantly in the seafloor. These characteristics vary temporally within a given mode. Both the dominant polarization angle and range of angles increase with frequency for observed *Ti* modes from earthquakes at widely varying distances and azimuths to H2O (Figure 6). The azimuth of propagation varies as well (not shown), with both near radial and wide angles (>30º) to radial. Some scatter may be expected from the sediment-basalt interface at ~30 m below the H2O sensors. However, observations of nanoearthquakes 3.7 km from the H2O site show simple waveforms not congruent with a strongly

heterogeneous local structure (Butler, 2003). Although the local receiver structure plays a significant role in the polarization angle, the observed variability of polarization characteristics for events at the nearly the same time, range and azimuth (e.g., the *Ti* mode at 10.7 Hz in Figure 5) suggests this cannot be the sole factor.

Given the sagittal and azimuthal variability of the polarization angles observed in the higher frequency (>5 Hz) *Ti* wave arrivals, in conjunction with the observed apparent velocity and dominance of the acoustic energy, local scattering is suggested to play a role in the *Ti* wave observations. The seafloor at the H2O site is very flat. Although there are abyssal hills less than 500 m above the seafloor at 30 km southwest of the H2O site, most of the seafloor in an area >5,000 km^2 around the site varies by less than 100 m from the H2O depth. Given the flatness of the seafloor in the region near the H2O site, contributions from acoustic scattering must somehow be manifested in the water above the H2O site.

The lowest frequency (<5 Hz) components of *Ti* waves have dominant energy in the sediments and propagate as seismoacoustic coupled modes. At frequencies above about 10 Hz, the hydroacoustic energy is dominant, and suggesting a contribution from local acoustic scattering. However, even these putative scattered arrivals set up local mode coupling (Figure 4). Scattering along the *T* wave propagation path potentially may insonify the seafloor, generating a spectrum of seismoacoustic coupled modes that propagate (*Ti*) at the seafloor. Whereas the lowest frequency interface modes may have propagated from the earthquake source region (Butler and Lomnitz, 2002), it is likely that there is also a contribution from insonification of the seafloor by acoustic scattering in the upper ocean along the path.

B. OSN1

The OSN1 pilot experiment (Stephen *et al.,* 2003) simultaneously recorded seismometers deployed on the seafloor, shallow buried in the sediments, and below the sediment-basalt interface during a six-month period in early 1998 (Figure 1). No hydrophone was deployed. Butler (2001) reported the observation of seismoacoustic *T* waves on the borehole seismometer as well as on the seafloor sensors, from local Hawaii Island earthquakes and from a single, large earthquake near the coast of Guatemala at more than 7000 km distant. Observations of *Ti* at both the OSN1B and OSN1 vertical sensors from the distant earthquake are shown in Figure 7. These arrivals are clearly discernible only when the data are high-pass (5 Hz) filtered. Given the 20 s^{-1} sampling and anti-aliasing filters on the data streams, the effective bandwidth of the OSN1 signal is only from 5 to 7 Hz. The signal-to-noise ratio on the OSN1B buried seismometer is substantial and comparable to H2O observations. Although the SNR for the OSN1 borehole seismometer is only about 2:1, the *Ti* wave arrives with no appreciable difference in time from its counterpart at the seafloor 242 m above.

Polarization of *Ti* is observed both on the shallow-buried OSN1B and the OSN1 borehole sensor from nearby, small (M=4) Hawaii Island earthquakes (*Butler,* 2001). The *Ti* observed on the OSN1B shallow-buried sensor shares many characteristics with its H2O counterpart. The energy is horizontally polarized, dominantly radial, and inclined <5° from the horizontal dipping downward and away from the source. However, the OSN1 borehole sensor indicates a different *Ti* polarization character—the energy is dominantly in the sagittal plane and vertically polarized. The *Ti* wave from the Guatemala earthquake shares this characteristic (Figure 8).

The propagation path of *Ti* from the Guatemala Earthquake to OSN1 presents an interesting puzzle, as show in Figure 9. The Island of Hawaii lies directly in the middle of the great circle propagation path. It is well known that islands may effectively block the propagation of SOFAR *T* waves. However, it is evident that *Ti* may still be observed at and beneath the seafloor of OSN1. The travel times of the *T* waves offer one clue, as shown in Figure 10. The OSN1 observation arrives about 30 sec late relative to island stations. Hence, it may be deduced that it did not travel through the Island of Hawaii (since conversion and transmission partly as a compressional wave within the Island would result as a faster, early arrival). About 10 seconds of the observed delay may be accounted from *T*-to-*P* conversion for the island stations.

The key to unraveling the observation of *Ti* from the Guatemala earthquake at OSN1 lies in polarization analysis of the OSN1B buried sensor (Figure 11), which displays a dominant polarization direction along in the azimuth 135.5°±180°. Rotating the coordinate frame along this azimuth and viewing the polarization with respect to the vertical component of motion, the horizontal polarization again dominates over the vertical motion with the direction of polarization inclined at about 3° from the horizontal, consistent with H2O observations in general and OSN1B observations from Hawaii earthquakes. If an apparent propagation direction from southeast to northwest is selected, then the orientation of the motion in this apparent sagittal plane is consistent with the other polarization observations, i.e., down and away from the apparent source.

South of Hawaii there are a number of seamounts that intersect the SOFAR channel which lie near the apparent azimuth of the OSN1 *Ti* observation from the Guatemala earthquake (Figure 9). The Cross Seamount (18°43'N, 158°17'W), which rises into the

SOFAR channel within 500 m of the sea surface, fits the approximate timing (+23 sec), but it is likely that the observed Ti signal at OSN1 is due to scattering from several seamounts.

III. Discussion

A. Interface Modes

The energy distribution and polarization characteristics of the low frequency (<~5 Hz) part of the *Ti* are consistent with Butler and Lomnitz (2002), who interpreted the seismoacoustic modes as energy trapped near the sediment-water interface by the low shear wave velocity of sediments. However, more recent observations permit another hypothesis. *Butler* (2003) modeled nanoearthquakes near the H2O site to obtain a first-order sediment and uppermost basalt velocity structure. The average shear wave velocity for the sediments is about 97 m/s. The basalt shear wave velocity—about 1.5 km/s—is slow for typical Eocene age (45-50 m.y.) sea floor, but consistent with observed pillow basalts recovered from the nearby ODP borehole 1.5 km northeast of H2O. Since the lower frequency modes (<10 Hz) have wavelengths (>150 m) much greater than the sediment thickness, which is 30 m or less, another possible interpretation for the observed seismoacoustic modes is that they are Scholte waves (fluid-solid interface Rayleigh waves) traveling at velocities just below the shear wave speed of the basalt basement. The close proximity of the basalt shear wave velocity to the acoustic water sound speed will potentially enhance this Scholte mode coupling. However, in either interpretation, the propagation characteristics of the low frequency *Ti* are higher-mode Rayleigh waves coupled between the seafloor and the water. Although these evanescent modes have been

observed within the basalt basement, the energy distribution throughout the water column is not known.

At the OSN1 site the observed polarization characteristics of *Ti* are consistent with the propagation of an evanescent wave. The vertical polarization of *Ti* observed on the OSN1 borehole seismometer located in the basalt is the same, whether from nearby Hawaii earthquakes or scattered from a seamount for the Guatemala event. For the seafloor-buried sensors at H2O and OSN1, the radial component dominates in the sediments. Crossing the sediment-basalt interface, the sagittal polarization of *Ti* rotates from radial to vertical. This is consistent with *Ti* propagation in the basalt layer as an evanescent mode balancing the vertical momentum of shallow-angle, post-critically reflecting waves propagating above the sediment-basalt interface (*e.g.,* Sykes and Oliver, 1964).

Only apparent velocity has been measured at H2O sea floor site. The apparent velocities measured at great distance over two different azimuths are both about 1.48 km/s, which is the characteristic of the low-velocity axis of the SOFAR channel, suggesting that the SOFAR axis participates in the propagation. However, it is not clear whether *Ti* is simply the sea floor expression of the family of modes encompassing the whole water column or whether *Ti* is locally generated from scattering out of the SOFAR channel near the H2O region and then propagates along the sea floor interface, or both. It is not clear whether the velocity observations are due to the SOFAR axis or shear wave velocity structure of the sea floor around the H2O site, or both. Detailed phase and group velocity from a horizontal seismoacoustic array, as well as observation of the acoustic wavefield throughout the water column from a vertical hydrophone array, would aid substantially in understanding the nature and propagation of these seismoacoustic modes.

B. Acoustic Scattering

By seismic reciprocity (*e.g.,* Aki and Richards, 1980), the interchangeability of source and receiver permits the observations of *Ti* scattered from the SOFAR channel to the seafloor to be viewed in reverse. The generation of *T* waves by earthquakes has long been a puzzle, particularly in the abyssal environment. Mechanisms proposed include down-slope conversion (*Tolstoy*, 1950), seafloor-seasurface reflection scattering (*Johnson et al.*, 1968), seafloor roughness scattering (*Fox et al.,* 1994*; de Groot-Hedlin and Orcutt,* 1999; *de Groot-Hedlin and Orcutt,* 2001), and modal scattering (*Park et al.*, 2001). The OSN1 *Ti* observation from the Guatemala earthquake appears to be due the scattering from a seamount (e.g., *Johnson et al.*, 1968). However, the limited data and the lack of a hydrophone do not permit a more detailed analysis about the nature of the scattering. For example, is the scattered energy dominantly in the water column, or has it propagated from the seamount as an interface wave (*Butler and Lomnitz,* 2002)? Seamount scattering cannot explain the H2O *Ti* observations. The marked consistency of the observed horizontal polarization within a few degrees of the back-azimuth to the earthquake source for all events observed cannot be mimicked by a plausible distribution of seamount scatters.

None of the other scattering mechanisms posited for the generation of abyssal *T* waves, except perhaps for sea surface scattering, can cause energy traveling in the SOFAR channel to be scattered to the sea floor as observed at H2O. In the case of sea surface roughness, for megameter scale *T* propagation it will contribute as a secondary scatterer for energy scattered to the sea surface by other processes.

The ocean is not perfectly transparent to acoustic energy, but the magnitudes and spatial structure of heterogeneities from physical oceanographic processes do not appear to be

sufficiently large to explain the *Ti* observations. Internal waves (Garrett and Munk, 1976) and their effect on acoustic scattering in the ocean have been known and studied since the 1970's (e.g., Munk and Zachariasen, 1972; Flatté *et al.*, 1979; Henyey and Macaskill, 1996). Numerical simulations (Colosi *et al.,* 1994, 1999) of acoustic propagation using environmental data from the SLICE89 (Duda *et al.,* 1992) experiment in the north-central Pacific which take into account internal-wave-induced sound-speed perturbations obeying the Garrett-Munk spectral model do predict some penetration of acoustic energy into the shadow zone, but not as deep as observed herein for H2O. Shadow zone arrivals (Spiesberger and Tappert, 1996) have been observed at a hydrophone array near the H2O site and at several other deep arrays in both the Atlantic and Pacific by *Dushaw et al*, (1999), who state "To date, no known mechanism, e.g., diffraction leakage from caustics or diffusion of acoustic energy by internal wave scattering, can explain the extreme diffusion of acoustic energy that must be occurring." Whereas the locally flat bathymetry will not substantially contribute as a local source for the internal wavefield (*e.g.,* St. Laurent and Garrett, 2003), tidal interactions with the Hawaiian Ridge at 1500 km distance have been found to be an important source of internal waves (Rudnick *et al.,* 2003) and could potentially increase acoustic scattering in the region of the H2O site. However, the observations of shadow zone arrivals at other deep hydrophone array sites (*e.g.,* Dushaw *et al.,* 1999) militate against this assumption.

Density-neutral thermohaline covariation—defined in terms of the variable, spice or spiciness, which increases for hot and salty water (Veronis, 1972; Munk, 1981)—is directly a measure of acoustic velocity heterogeneity, since the effects of temperature and salinity both correlate positively on acoustic velocity. Thermohaline fine structure has been

observed near the H2O site from a physical oceanographic survey in early 1997 (*Rudnick and Ferrari,* 1999; *Ferrari and Rudnick,* 2000), and from marine seismic reflection profiling (*Holbrook et al.,* 2003) in the Atlantic. Dzieciuch *et al.* (2003) present a thorough analysis of the 1997 Spice Experiment data set, separating internal wave and spice contributions. Spiciness dominates internal wave contributions to sound speed perturbations in the upper mixed layer, but RMS differences over 3 km scales are relatively small, ~0.35 m/s. Beneath the mixed layer at 200 m, internal waves dominate spice, with RMS differences of 0.74 m/s and 0.35 m/s respectively. Numerical simulations of acoustic propagation through the structure do not indicate substantial penetration of acoustic energy into the shadow zone (M. Dzieciuch, personal communication, 2003).

Unlike spice and internal waves which both deflect ray paths over small angles, acoustic bio-scattering from large fish and marine mammals offers a means to explain the high angle scattered energy observed in Figure 6. Low-frequency Rayleigh scattering from a single fish or marine mammal is significant near the swimbladder or lung resonance frequency, respectively (*e.g., Love,* 1978). These scatterers act omni-directionally, but fall off asymptotically as $\sim f^{-4}$ below the resonance peak. A scattering model developed for schools of fish predicts a broadening of the resonance and a shift of the peak to lower frequency (*Feuillade et al.,* 1996). *Nero* (1996) has modeled acoustic scattering from schools of up to 1400 large tuna, for school radii up to ~100 m. Large schools of tuna with dimensions 100s m laterally and vertically have been observed by professional fishermen in the Hawaiian Islands region (*B. Kam,* personal communication, 2003). For an individual 80 cm yellowfin tuna, the target strength (TS) is -13 dB at resonance f=220 Hz, and TS < -60 dB for f < 40 Hz. However, for schools of more than 300 tuna, the TS is ~ -50 dB at

15 Hz (*Nero,* 1996). Larger tuna (up to 150 cm fork length) will have lower frequency resonances (down to 110 Hz) (*Schaefer and Oliver*, 2000). Marine mammals have lower resonant frequencies, and consequently are much better scattering sources at low frequency. *Finneran* (2003) measured *in vivo* lung resonant frequencies of 30 and 36 Hz (TS ~ 0 dB) for a 540 kg white whale and a 280-kg dolphin, which follows the terrestrial mammal mass-frequency relation of $f \sim M^{-1/4}$. For a 126-kg dolphin, *Au* (1996) measured a resonance near 23 Hz and TS ~ -11 dB. Since the resonance frequency is a strong function of depth (both lung and swimbladder volumes diminish with depth), at *Ti* wave frequencies the dominant contribution from bio-scattering will come from the upper mixed layer, <50 m. For comparable numbers, large marine mammals individually and in pods will have a much greater acoustic scattering effect than tuna and schools thereof.

The significance of bio-scattering may be judged in relation to spice and internal wave scattering. Holbrook *et al.* (2003) note that the strongest reflection coefficients from thermohaline (spice) reflectors have an acoustic wave speed contrast of 15 m/s at 0.005, which corresponds to a target strength of -46 dB. For sound speed changes of 0.3 m/s (roughly the RMS fluctuations determined by Dzieciuch *et al.* (2003) for the 1997 Spice experiment), the reflection coefficient 0.0001 has a TS of -80 dB. It is clear that individuals and schools of tuna and pods of marine mammals *may* contribute to the scattering observed in this *Ti* data set, compared with spice and internal waves. Rayleigh bio-scattering will occur as the *T* wave propagates throughout the upper mixed layer (< 100 m) of the ocean as it interacts with the populations of large marine animals. Each interaction of the incident *T* wave signal upon the marine population is a new source of scattered *T* wave energy contributing to the wavefield, and the effect on the sea floor at the H2O site is the sum over

all these Rayleigh scattered sources close to and distant from H2O each convolved with the Green's Function for the acoustic ocean propagation.

Whereas the possible influence of acoustic bio-scattering by a substantial population of large marine mammals remains intriguing, there are no population census data which can be used draw any conclusions. Whales are routinely observed to migrate seasonally through the H2O site region based upon whale calls observed. If a correlation could be shown between whale migration times and *Ti* signal strength, then a more plausible connection might be inferred for the acoustic bio-scatter contribution.

None of the scattering mechanisms—internal waves, spice, acoustic bio-scatter, sea surface and sea floor roughness—appear to be sufficiently robust to scatter energy from the SOFAR channel to the deep sea floor beneath the conjugate depth at the H2O site. Yet strong *Ti* arrivals are observed on the sea floor with distinctive, characteristic energy distributions and polarizations traveling with apparent velocities appropriate for SOFAR *T* waves. Obviously, better instrumentation from the sea floor throughout the water column would provide better observational constraints. However, the problem is not lack of observations, it is the lack of a reasonable model to explain the observations. Without a better model, it seems reasonable to call into question the limitations being placed upon the known scattering mechanisms: are the velocity perturbations and scattering populations being somehow underestimated?

IV. Conclusions

The combination of a hydrophone above the sea floor with broadband seismic instrumentation within the sediments and in the basalt beneath the sea floor provide strong,

new observational constraints on the propagation of *T* waves within the ocean. These seismoacoustic, interface *Ti* waves are routinely observed in the shadow-zone of *T* wave propagation, traveling with apparent velocities appropriate for the SOFAR channel. Substantial energy propagates in the sea floor at low (<5 Hz) frequencies, and the energy distribution and polarization characteristics indicate higher-mode Rayleigh/Scholte wave propagation. At frequencies above 5 Hz the energy distribution and polarization characteristics of *Ti* suggest a contribution from acoustic scattering processes in the upper ocean. By reciprocity, such scattering mechanisms may contribute to the generation of *T* waves near the earthquake source. However, none of the scattering mechanisms individually appear to be sufficiently robust to explain the H2O observations.

Acknowledgments. Supported by NSF Cooperative Agreement EAR-0004370. I have enjoyed discussions with Walter Munk, John Colosi, Matt Dzieciuch, Dan Rudnick, Bruce Howe, Brian Dushaw, Neil Frazer, Whitlow Au, Brian Kam, Henrik Schmidt, and Fred Duennebier who have sharpened my appreciation of the mysteries of acoustic wave scattering in the ocean, marine life, and Scholte modes. I thank Cecily Wolfe for Pelenet data. I thank Bill Siegmann for constructive suggestions in focusing this manuscript. SOEST contribution number XXX.

References

Aki, K., and P. G. Richards (**1980**). Quantitative Seismology, 932 pp., W. H. Freeman & Company, New York, New York.

Au, W. L, Acoustic Reflectivity of a Dolphin (**1996**). *J. Acoust. Soc. Am., 99,* 3844-3848.

Butler, R., A. D. Chave, F. K. Duennebier, D. R. Yoerger, R. Petitt, D. Harris, F. B. Wooding, A. D. Bowen, J. Bailey, J. Jolly, E. Hobart, J. A. Hildebrand, and A. H. Dodeman (**2000**). Hawaii-2 Observatory pioneers opportunities for remote instrumentation in ocean studies, *Eos, 81*, 157-163.

Butler, R. (**2001**). Observation of seismo-acoustic T phases at and below the seafloor in the Northeastern Pacific at the Hawaii-2 Observatory and OSN1 site, *EOS Trans AGU, 82 (47),* Fall Meet. Suppl. Abstract S21A-0557.

Butler, R, and C. Lomnitz (**2002**). Coupled seismoacoustic modes on the seafloor, *Geophys. Res. Lett., 29(10)*, 57 1-4, doi:10.1029/2002GL014722.

Butler, R. (**2003**). The Hawaii-2 Observatory: Observation of Nanoearthquakes, *Seismol. Res. Lett., 74(10),* 290-297.

Butler, R and T. Lay, K. Creager, P. Earl, K. Fischer, J. Gaherty, G. Laske, W. Leith, J. Park, M. Ritzwoller, J. Tromp, L. Wen (**2004**). The Global Seismographic Network surpasses its design goal, *EOS Trans AGU, in press*.

Colosi, J. A., S. M. Flatté, and C. Bracher (**1994**). Internal-wave effects on 1000-km oceanic acoustic pulse propagation: Simulation and comparison with experiment, *J. Acoust. Soc. Am., 96*, 452-468.

Colosi, J. A., and the ATOC Group (A. B. Baggeroer, T. G. Birdsall, C. Clark, J. A. Colosi, B. D. Cornuelle, D. Costa, B. D. Dushaw, M. Dzieciuch, A. M. G. Forbes, B. M. Howe, D. Menemenlis, J. A. Mercer, K. Metzger, W. H. Munk, R. C. Spindel, P. F. Worcester, C. Wunsch) (**1999**). A review of recent results on ocean acoustic wave propagation in random media: Basin scales, *IEEE J. Oceanic Eng., 24(2),* 138-155.

de Groot-Hedlin, C, and J. A. Orcutt (**1999**). Synthesis of earthquake-generated *T*-waves, *Geophys. Res. Lett., 26(9),* 1227-1230.

de Groot-Hedlin, C, and J. A. Orcutt (**2001**). Excitation of *T*-phases by seafloor scattering, *J. Acoust. Soc., Am., 109,*, 1944-1954.

Duda, T.F., S.M. Flatté, J.A. Colosi, B.D. Cornuelle, J.A. Hildebrand, W.S. Hodgkiss, P.F. Worcester, B.M. Howe, J.A. Mercer, and R.C. Spindel (**1992**). Measured wavefront fluctuations in 1000 km pulse propagation in the Pacific Ocean, *J. Acoust. Soc. Am ., 92* , 939-955.

Dushaw, B. D., B. M. Howe, J. A. Mercer, and R. C. Spindel (**1999**). Multimegameter-range acoustic data obtained by bottom-mounted hydrophone arrays for measurement of ocean temperature, *IEEE J. Oceanic Eng., 24*, 202-214.

Dushaw, B. D. (**1999**). Inversion of multimegameter-range acoustics data, *IEEE J. Oceanic Engineering, 24*, 215-223.

Dzieciuch, M., W. Munk, and D. L. Rudnick (**2004**). The propagation of sound through a spicy ocean; the SOFAR overture, *J. Acoust. Soc. Am ., in press.*

Finneran, J. L. (**2003**). Whole-lung resonance in a bottlenose dolphin (Tursiops truncatus) and white whale (Delphinapterus leucas), *J. Acoust. Soc. Am., 114(1)*,530-535.

Ferrari, R. and D. L. Rudnick (**2000**). Thermohaline variability in the upper ocean, *JGR*, *105*, C7, 16857-16883.

Feuillade, C., R. W. Nero, and R. H. Love (**1996**). A low frequency acoustic scattering model for small schools of fish, *J. Acoust. Soc. Am., 99(1),* 196-208.

Flatté, S. M., R. Dashen, W. Munk, K. Watson, F. Zachariasen (**1979**). *Sound Transmission through a Fluctuating Ocean,* Cambridge Univ. Press, Cambridge.

Fox, C. G., R. P. Dziak, H. Matsumoto, and A. E. Schreiner (**1994**). Potential for monitoring low-level seismicity on the Juan de Fuca Ridge using military hydrophone arrays, *Mar. Technol. Soc. J., 27,* 22-30.

Fox, C. G., H. Matsumoto, and T.-K.A. Lau (**2001**). Monitoring Pacific Ocean seismicity from an autonomous hydrophone array, *J. Geophys. Res., 106*, 4183-4206.

Henyey, F. S. and C. Macaskill (**1996**). Sound through the internal wave field, in *Stochastic Modeling in Physical Oceanography*, Birkhauser, Boston MA, pp 141-184.

Holbrook, W. S., P. Paramo, S. Pearse, and R. W. Schmitt (**2003**). Thermohaline fine structure in an oceanographic front from seismic reflection profiling, *Science , 301*, 821-824.

Johnson, R. H., R. A. Norris, and F. K. Duennebier (**1968**). Abyssally generated *T* phases, in *The crust and upper mantle of the Pacific area*, edited by L. Knopoff, C. L. Drake, and P. J. Hart, pp. 70-78, AGU Monograph.

Levitus, S., R. Burgett, and T. P. Boyer (**1994**). World Ocean Atlas 1994, Vol. 3: Salinity, NOAA Atlas NESDIS 3, U.S. Government Printing Office, 99pp, Washington DC.

Levitus, S. T.P. and Boyer (**1994**). World Ocean Atlas 1994, Vol. 4. Temperature, NOAA Atlas NESDIS 4, U.S. Government Printing Office, 117pp, Washington DC.

Love, R. H. (**1978**). Resonant acoustic scattering by swimbladder-bearing fish, *J. Acoust. Soc. Am., 64*, 571-580.

Munk, W. H. and F. Zachariasen (**1972**). Sound fluctuation through stratified ocean, *J. Acoust. Soc. Am., 59*, 818-838.

Munk, W. (**1981**). Internal waves and small scale processes, in *Evolution of Physical Oceanography: Scientific Surveys in Honor of Henry Stommel,* edited by B. A. Warren and C. Wunsch, pp 264-291, MIT Press, Cambridge, MA.

Nero, R. W. (**1996**). Model estimates of acoustic scattering from schools of large yellowfin tuna. *Report NRL/MR/774-95-7708*. Naval Research Lab. Stennis Space Center, MS. 21p,.

Okal, E. A. (**2001**). T-phase stations for the International Monitoring System of the Comprehensive Nuclear Test-Ban Treaty: A global perspective, *Seismol. Res. Lett., 72*, 186-196.

Park, M., R. I. Odom, and D. J. Soukup (**2001**). Modal scattering: the key to oceanic *T*-waves, *Geophys Res. Lett., 28(17)*, 3401-2404.

Rudnick, D. L., and R. Ferrari (**1999**). Compensation of horizontal Temperature and salinity gradients in the ocean mixed layer, *Science*, *283*, 526-529.

Rudnick D. L., T. J. Boyd, R. E. Brainard, G. S. Carter, G. D. Egbert, M. C. Gregg, P. E. Holloway, J. M. Klymak, E. Kunze, C. M. Lee, M. D. Levine, D. S. Luther, J. P. Martin, M. A. Merrifield, J. N. Moum, J. D. Nash, R. Pinkel, L. Rainville, T. B. Sanford (**2003**). From tides to mixing along the Hawaiian Ridge, *Science*, *301*, 355-357.

Schaefer, K. M. and C. W. Oliver (**2000**). Shape, volume, and resonance frequency of the swimbladder of yellowfin tuna, *Thunnus albacares*, *Fish. Bull., 98*, 364–374.

Spiesberger, J.L. and F. Tappert (**1996**). Kaneohe acoustic thermometer further validated with rays over 3700 km and the demise of the idea of axially trapped energy, *J. Acoust. Soc. Am., 99*, 173-84.

Stephen, R. A., F. N. Spiess, J. A. Collins, J. A. Hildebrand, J. A. Orcutt, K. R. Peal, F. L. Vernon, F. B. Wooding (**2003**). Ocean Seismic Network Pilot Experiment, Geochem. Geophys. Geosyst., *4(10)*, 1092, DOI 10.1029/2002GC000485.

Stephen, R.A., J. Kasahara, G. D. Acton, *et al.*, (**2003**). Proc. ODP, Init. Repts., 200 (CD-ROM). Available from: Ocean Drilling Program, Texas A&M University, College Station TX 77845-9547, USA.

St. Laurent, L. and C. Garrett (**2002**). The role of internal tides in mixing the deep ocean, *J. Phys. Oceanogr., 32* , 2882-2899.

Sykes, L. R. and J. Oliver (**1964**). The propagation of short period seismic surface waves across oceanic areas, Part I—Theoretical Study, *Bull. Seism. Soc. Am., 54(5),* 1349-72.

Tolstoy, I, and M. Ewing (**1950**). The *T* phase of shallow-focus earthquakes, *Bull. Seism. Soc. Am., 40*, 25-51.

Veronis, G. (**1972**). On properties of seawater defined by temperature, salinity, and pressure, *J. Mar. Res.*, *30*, 227-255.

Wolfe, C. J., S. C. Solomon, P. G. Silver, R. M. Russo, and J. C. VanDecar (**2002**). Inversion of body wave delay times for mantle structure beneath the Hawaiian islands: Results from the PELENET experiment, *Earth Planet. Sci. Lett., 198,* 129-145.

Figure 1. *T* waves are the most energetic arrivals at frequencies greater than 1 Hz on the hydrophone and the buried seafloor seismometer at the H2O site, and have been observed from events at distances of nearly 10,000 km. *T* waves have also been observed at OSN1 site, both on the buried seafloor seismometer and on the borehole seismometer 245m below the seafloor below the sediment-basalt interface. Locations of earthquakes discussed in the paper are noted.

Figure 2. *T* waves recorded on the seismometer and hydrophone at H2O have an apparent velocity of about 1.48 km/s, corresponding with the velocity near the axis of the SOFAR channel 4 km above the seafloor site. (above) An earthquake (magnitude Mw=6.7) on the South Pacific Ridge at 9400 km on August 8, 2001. Uncertainty of apparent velocity is estimated from epicentral uncertainty. (below) An earthquake (Mw=6.5) near the coast of Kamchatka at a distance of 5440 km on October 8, 2001. Radial components are shown successively high-pass filtered in three stages; the hydrophone is high-pass filtered at 5 Hz. The seismic wave field is polarized, and only the largest component, Radial, is shown.

Figure 3. Spectragrams plot energy versus frequency and time corresponding to the two events in Figure 1. The four plots (left to right) show the hydrophone, and seismic vertical, radial and tangential components of motion, respectively, all at the same scale for a given event. At frequencies below about 5 Hz, the total energy on the seismic components in the seafloor sediment is greater that on the hydrophone located in the water only 0.5 m above the seafloor. However, at higher frequencies, the power in the hydrophone signal is greater.

The banded structure in the seismic traces is indicative of modal coupling to the seafloor sediments. The hydrophone shows both modal structure and scattered energy.

Figure 4. *Ti* polarization of October 8, 20001 earthquake near Kamchatka from the Guralp seismometer buried in sediments. Acceleration records are normalized for instrument response, high pass filtered at 5 Hz. Left is vertical and radial, right is radial and tangential. Both are at the same scale for direct comparison. Positive radial is toward the source, positive tangential is +90 degrees clockwise from the radial. Dotted lines show the least-squares fitting line, computed iteratively without assuming either axis as the dependent or independent variable.

Figure 5. Examples of *Ti* polarization observations in the sagittal plane are shown for three frequency bands from events shown in Figures 1 and 2. The upper and lower examples are from the earthquake near Kamchatka, whereas the middle example is from the southern East Pacific Rise earthquake. The lowest frequency is polarized within 1º of horizontal and displays elliptical particle motion characteristic of seismoacoustic coupled Rayleigh waves. Higher frequency bands display a wide range of steeper polarization angles, and both elliptical and rectilinear particle motions characteristic of acoustic energy from the upper ocean being scattered incident upon and coupling to the seafloor. The middle and upper observations show average polarizations at 9.5º and 40.9º, respectively, from horizontal.

Figure 6. The polarization (radial-vertical) angles of individual *Ti* modes are shown as a function of frequency for four earthquakes. Positive angle is down and radially away from the source. The southern East Pacific Rise and first near Kamchatka events are shown in

earlier Figures. The second event near Kamchatka (Mw=6.4) occurred 6 minutes after the first and at the same location (distance and azimuth within 0.02% of first event from H2O). The Blanco Fracture Zone earthquake (Mw=6.2) on June 2, 2000 occurred at a distance of 2130 km northeast of H2O. Low frequency modes (<5 Hz) have near radial orientation whereas higher frequencies (>5 Hz) show increasingly steeper angles and greater scatter. Symbols are plotted at the polarization of the maximum energy, lines indicate range of polarization of modal frequencies. Small variations in frequencies of individual modes are observed between events. Note polarization variation of *Ti* mode at 10.7 Hz between the first and second earthquakes near Kamchatka, which have almost identical paths.

Figure 7. *Ti* is observed from an earthquake near Guatemala on the OSN1 borehole seismometer 245m below the OSN1B seafloor-buried sensor. A seismometer sitting on the seafloor (OSN1S), which also clearly observed *Ti*, is not shown. Data have limited bandwidth due to 20 sps sampling. The vertical-component records shown are not corrected for instrument response—digital amplitude counts are nominal. The *Ti* amplitude (velocity response) on OSN1 is about 30% of OSN1B. Although many Ti are observed from local Hawaii events during the six-month Ocean Seismic Network (OSN) Pilot Experiment, this is the only circum-Pacific event seen. Remarkably, the great circle propagation path from the Guatemala event to OSN1 is blocked by the Big Island of Hawaii.

Figure 8. Observation of vertically-polarized *Ti* from the Guatemala earthquake on the vertical and horizontal components of OSN1 borehole sensor, high-pass filtered at 5 Hz. Horizontal components have been rotated into orthogonal azimuths determined from

OSN1B sensor polarization (Figure 11), and normalized to the vertical (BHZ) instrument response.

Figure 9. The great circle paths (yellow) from the Guatemalan Earthquake to OSN1 and Hawaiian Islands seismic stations are shown. The apparent great circle to OSN1 is blocked by the big Island of Hawaii. The apparent propagation direction of *Ti* derived from polarization analysis (Figure 12) is shown as the red line. The green lines indicate propagation delays for paths scattered from seamounts to the southeast.

Figure 10. The travel times of *T* waves are plotted for the sites in Figure 10. The travel time corresponds to the maximum of the low-pass filtered envelope of the respective *T* wave. Note that the OSN1 arrival is delayed by about 30 seconds relative to the Hawaiian Island observations: Pelenet sites (Wolfe *et al.,* 2002) and the GSN station KIP on Oahu.

Figure 11. *Ti* polarization for Guatemala earthquake observed at the OSN1B shallow buried sensor, high-pass filtered at 5 Hz. The right figure shows horizontal components as oriented *in situ.* Dotted lines show the least-squares fitting line oriented at 135.5°, computed iteratively without assuming either axis as the dependent or independent variable. Left figure is vertical and horizontal rotated into an orientation at 135.5°. Both are at the same scale for direct comparison. Based upon consistency with observed H2O polarizations, the *Ti* arrival at OSN1B appears to be propagating from an azimuth 135.5° towards the northwest.

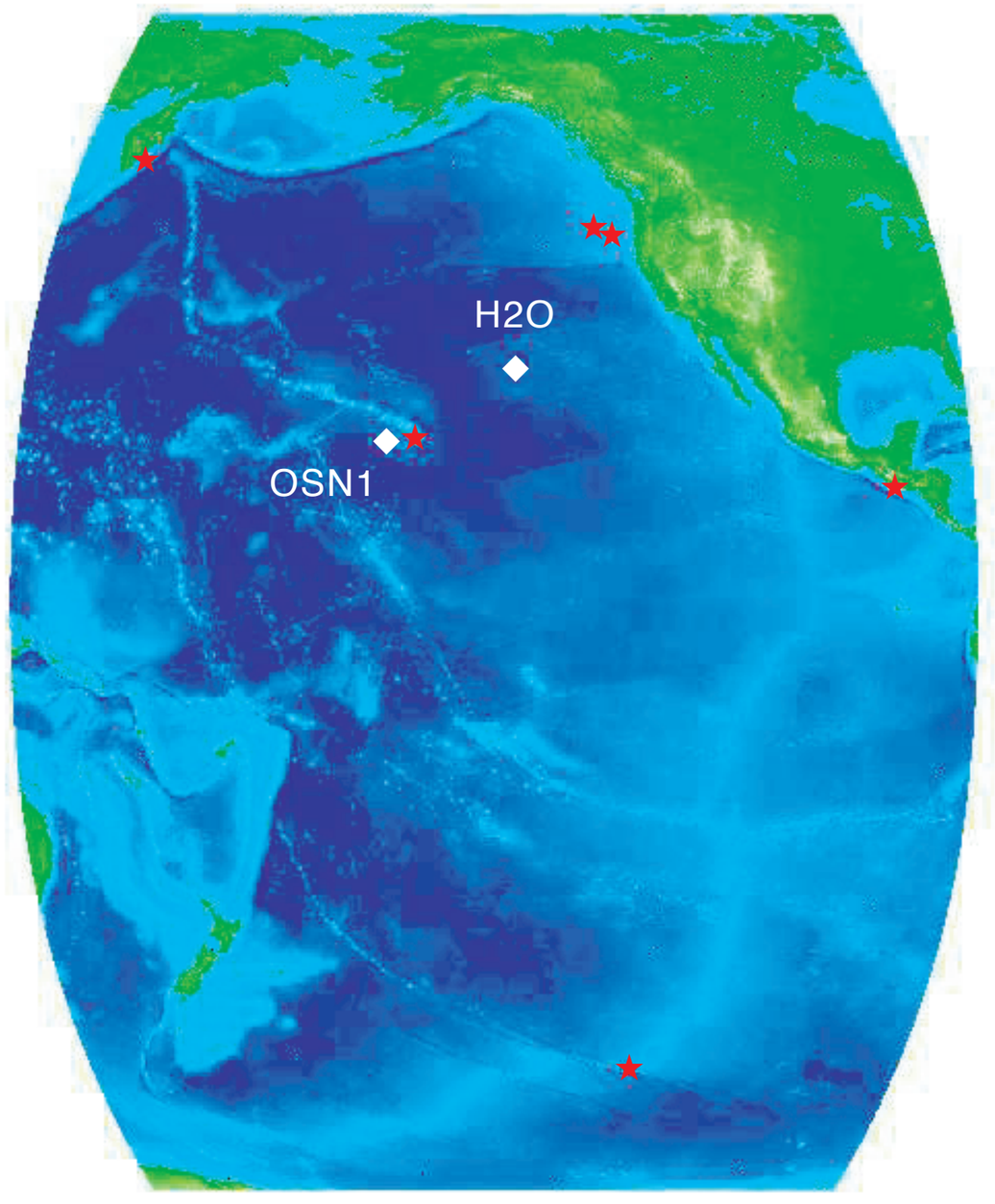

Figure 1.

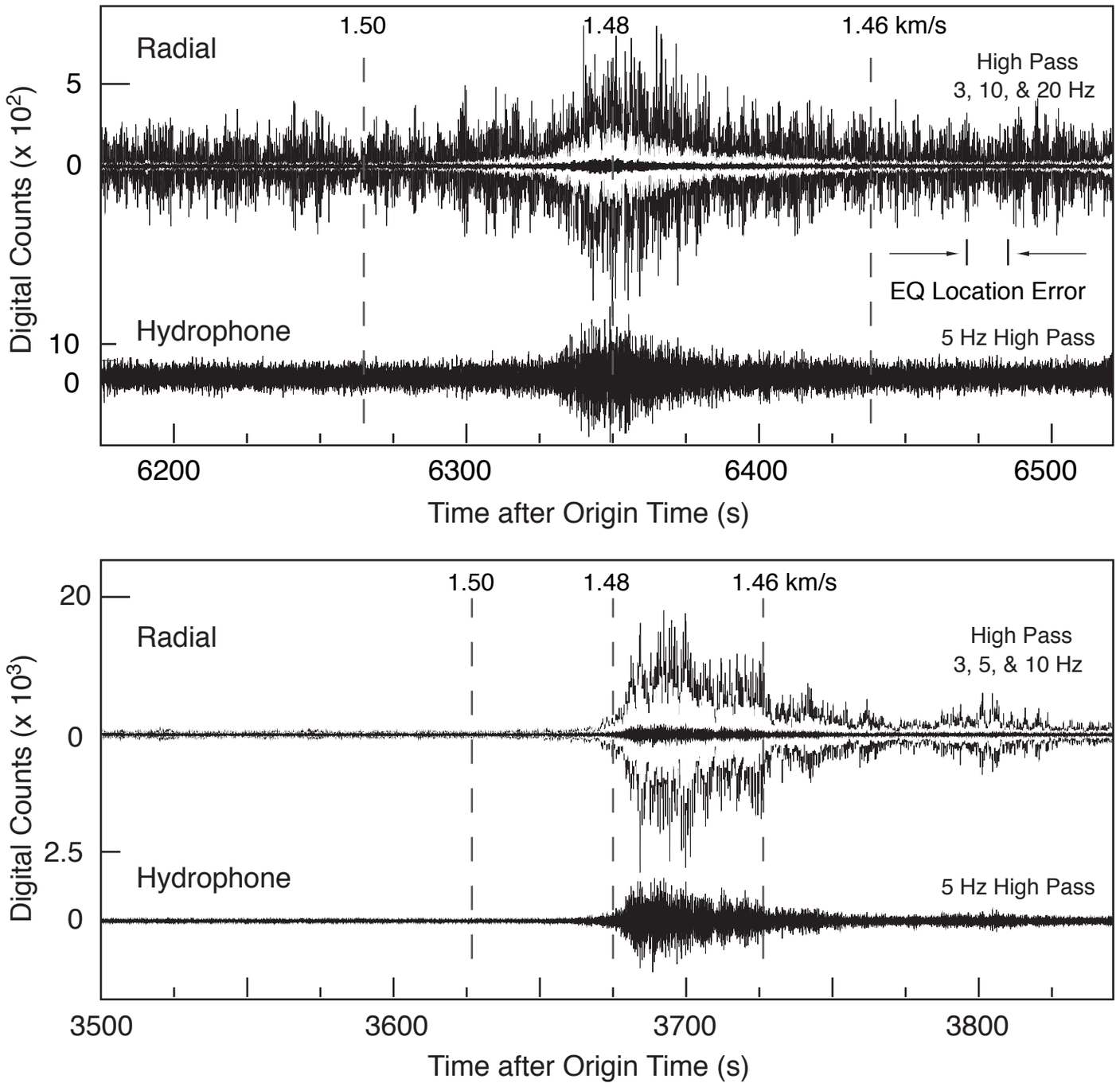
1.50
1.48
1.46 km/s
Radial
High Pass
3, 10, & 20 Hz
5
0
Digital Counts (x 10²)
EQ Location Error
Hydrophone
5 Hz High Pass
10
0
6200
6300
6400
6500
Time after Origin Time (s)
1.50
1.48
1.46 km/s
20
Radial
High Pass
3, 5, & 10 Hz
0
Digital Counts (x 10³)
2.5
Hydrophone
5 Hz High Pass
0
3500
3600
3700
3800
Time after Origin Time (s)

Figure 2.

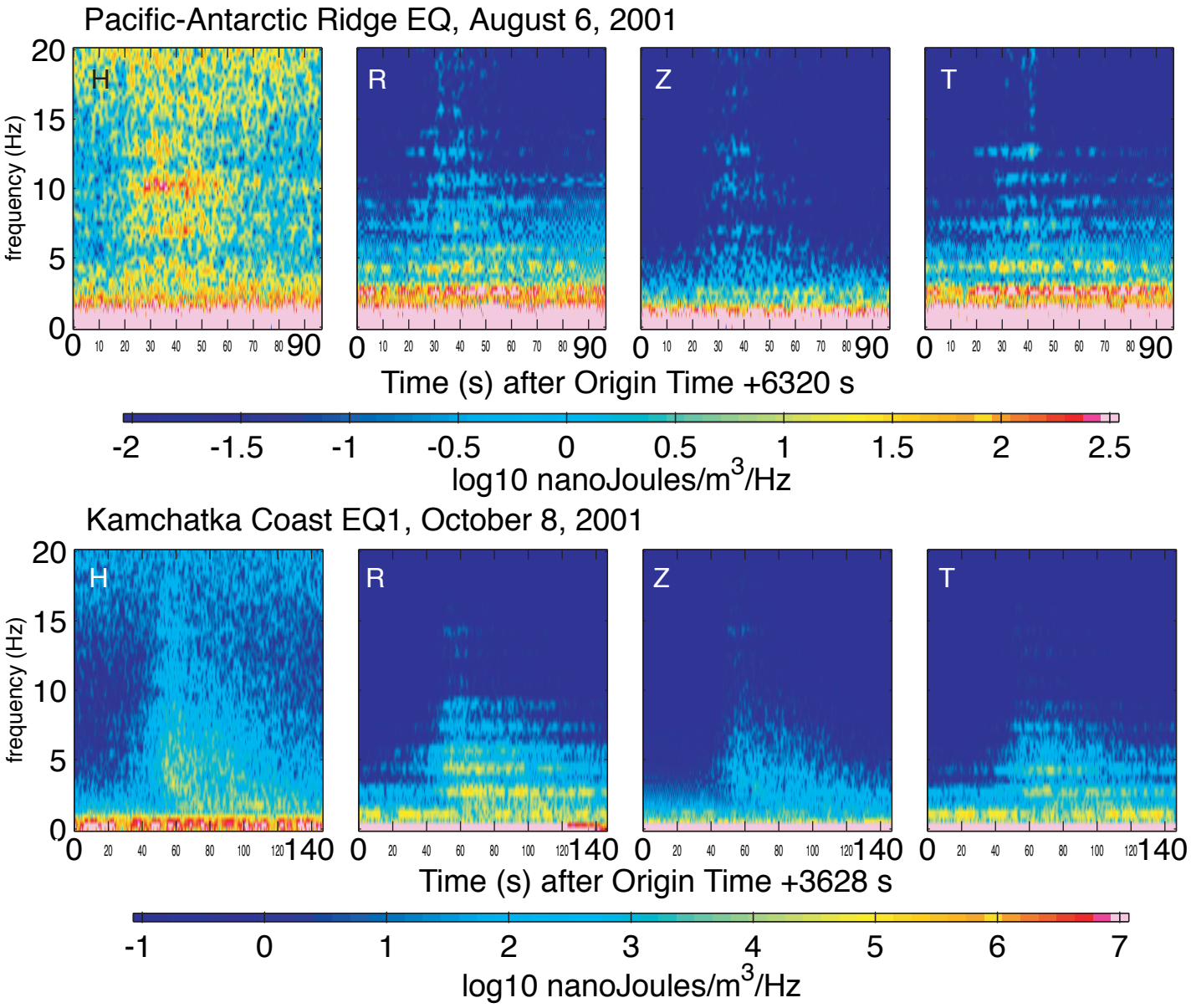
Pacific-Antarctic Ridge EQ, August 6, 2001
H
R
Z
T
frequency (Hz)
Time (s) after Origin Time +6320 s
log10 nanoJoules/m3/Hz
Kamchatka Coast EQ1, October 8, 2001
Time (s) after Origin Time +3628 s
log10 nanoJoules/m3/Hz

Figure 3.

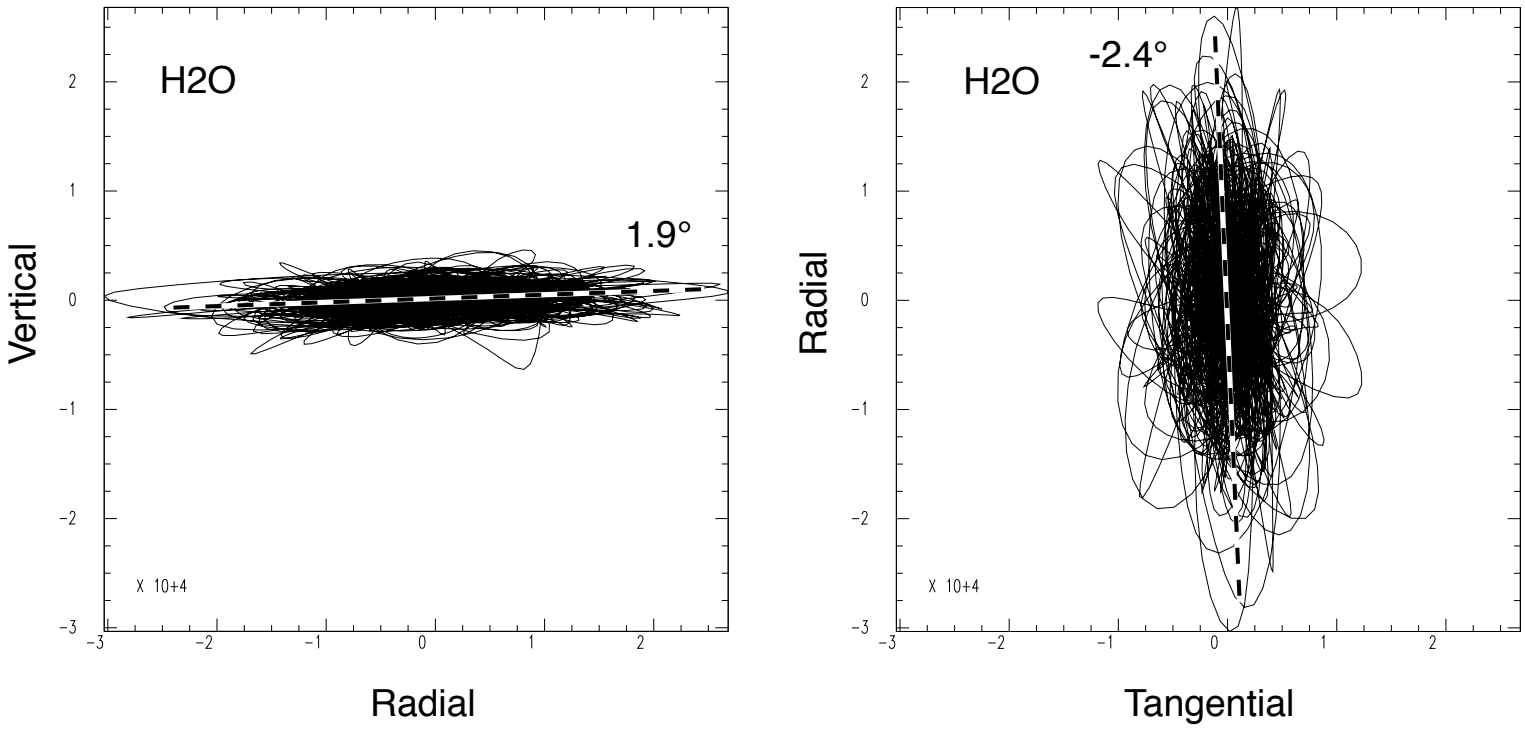

Figure 4.

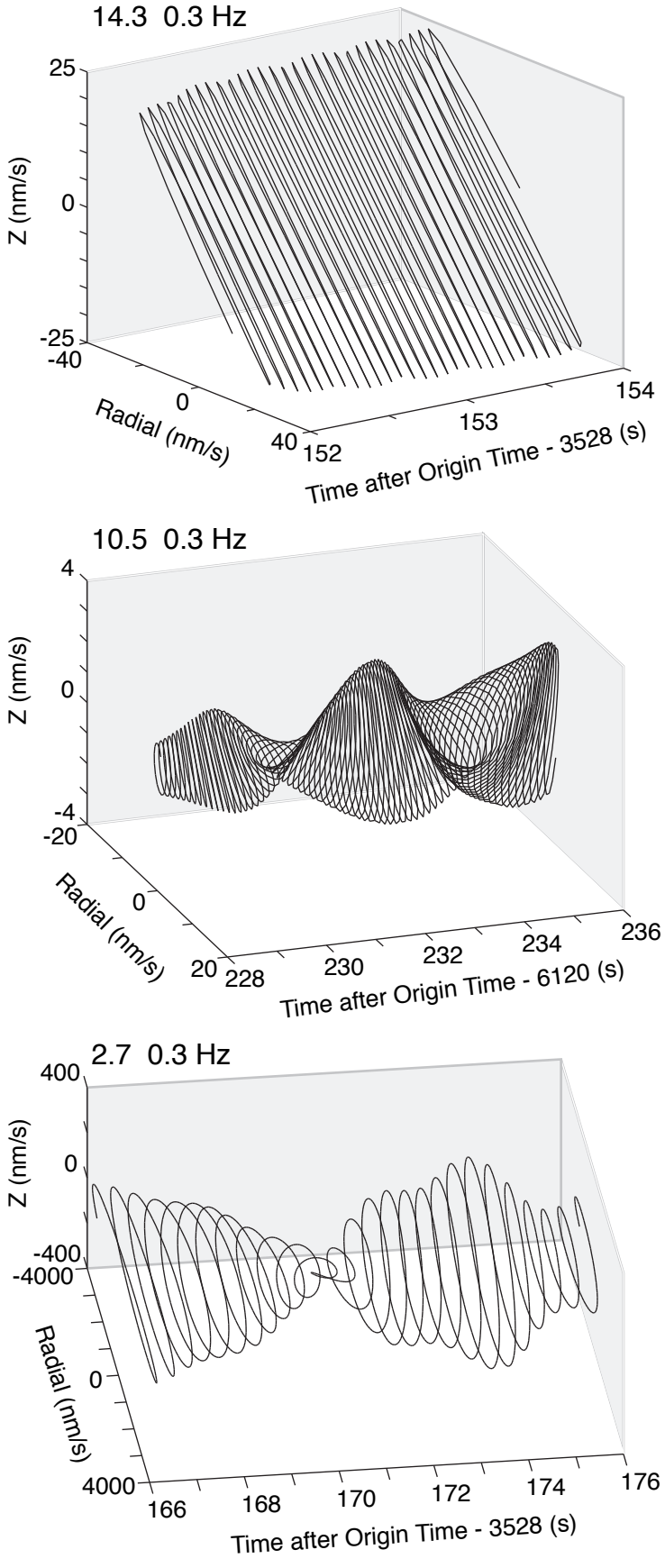
14.3 0.3 Hz
25
0
-25
Z (nm/s)
-40
0
40
Radial (nm/s)
152
153
154
Time after Origin Time - 3528 (s)
10.5 0.3 Hz
4
0
-4
Z (nm/s)
-20
0
20
Radial (nm/s)
228
230
232
234
236
Time after Origin Time - 6120 (s)
2.7 0.3 Hz
400
0
-400
Z (nm/s)
-4000
0
4000
Radial (nm/s)
166
168
170
172
174
176
Time after Origin Time - 3528 (s)

Figure 5.

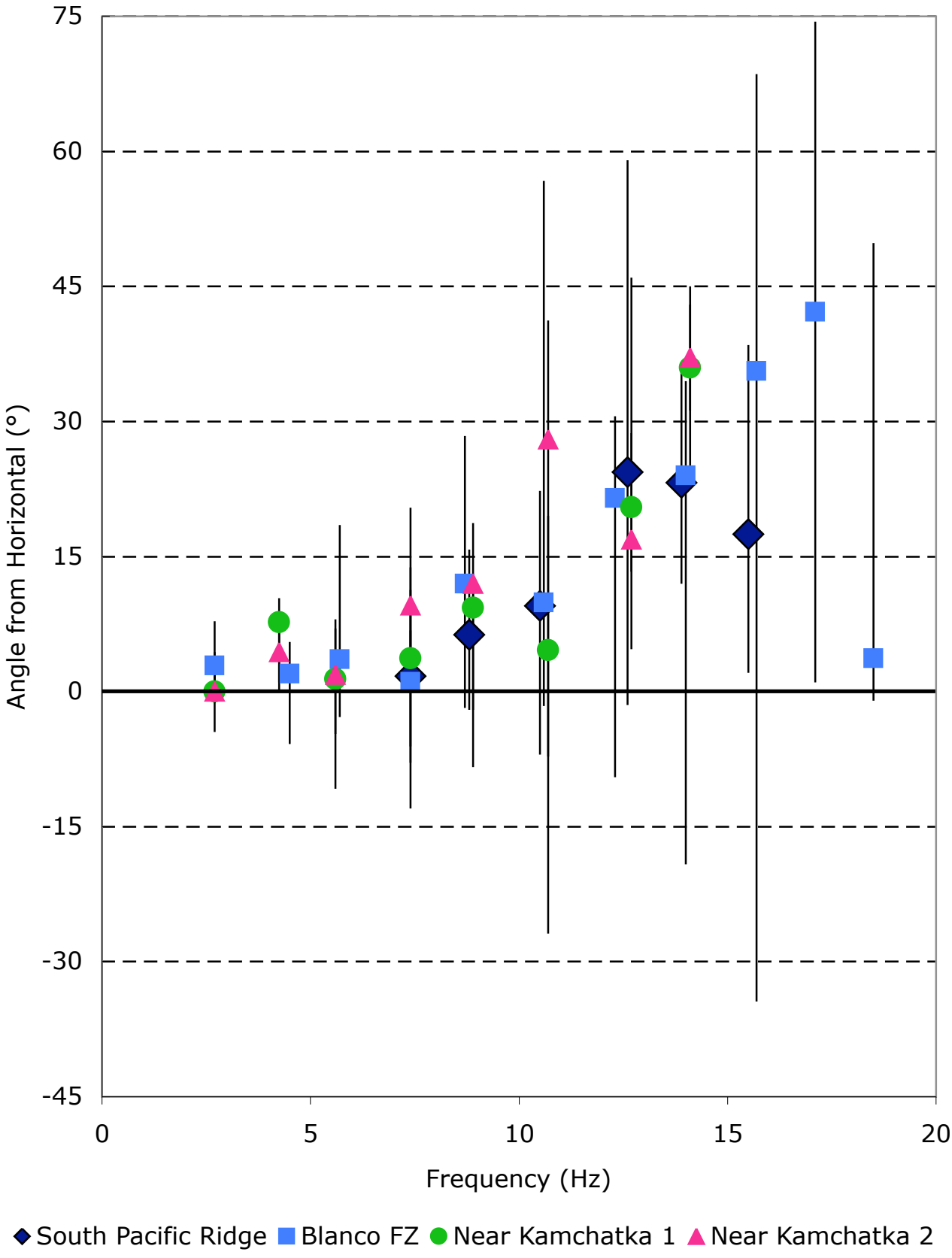
75
60
45
30
15
0
-15
-30
-45
Angle from Horizontal (°)
0
5
10
15
20
Frequency (Hz)
South Pacific Ridge
Blanco FZ
Near Kamchatka 1
Near Kamchatka 2

Figure 6.

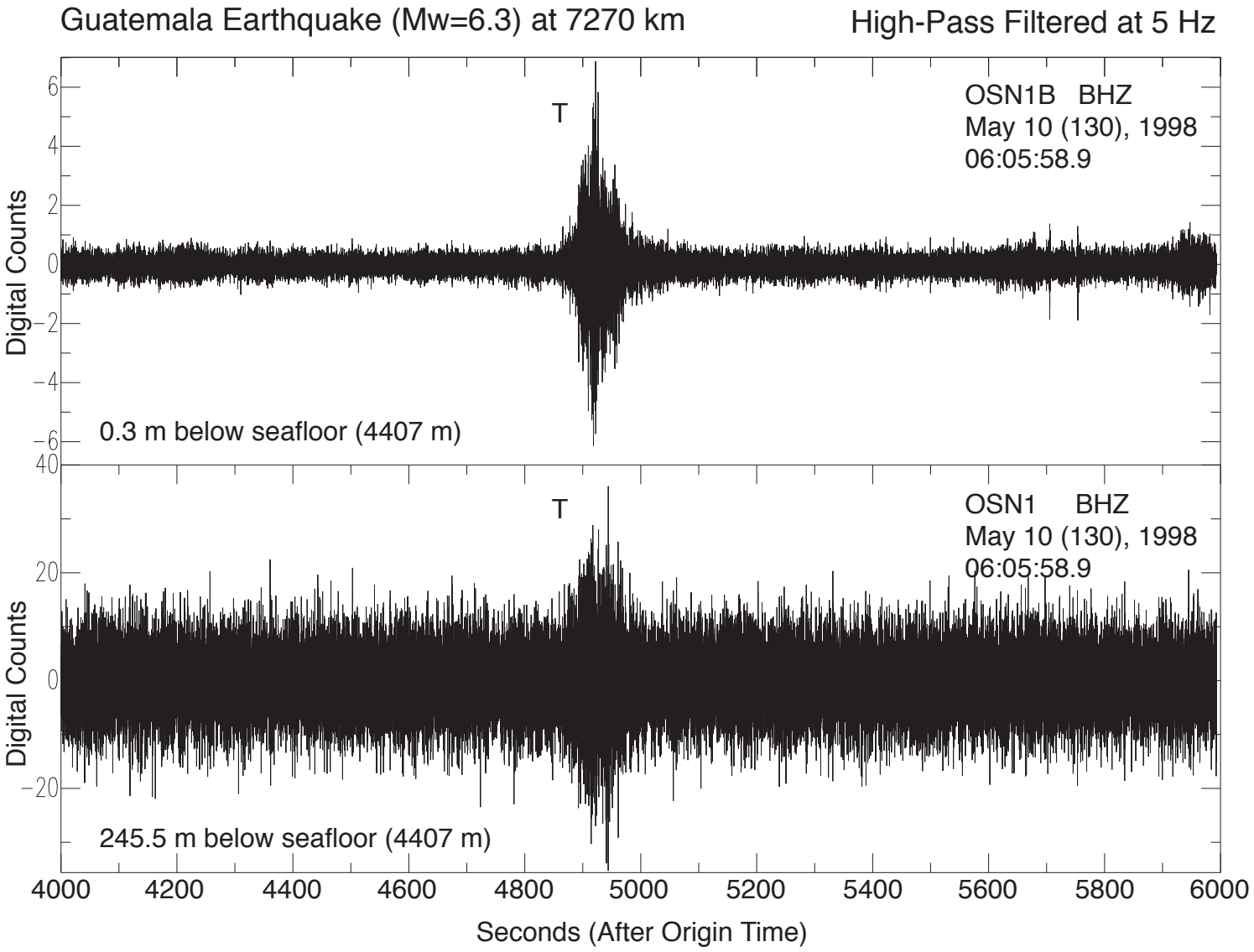
Guatemala Earthquake (Mw=6.3) at 7270 km
High-Pass Filtered at 5 Hz
OSN1B BHZ
May 10 (130), 1998
06:05:58.9
T
0.3 m below seafloor (4407 m)
OSN1 BHZ
May 10 (130), 1998
06:05:58.9
T
245.5 m below seafloor (4407 m)
Digital Counts
Digital Counts
Seconds (After Origin Time)
4000
4200
4400
4600
4800
5000
5200
5400
5600
5800
6000

Figure 7.

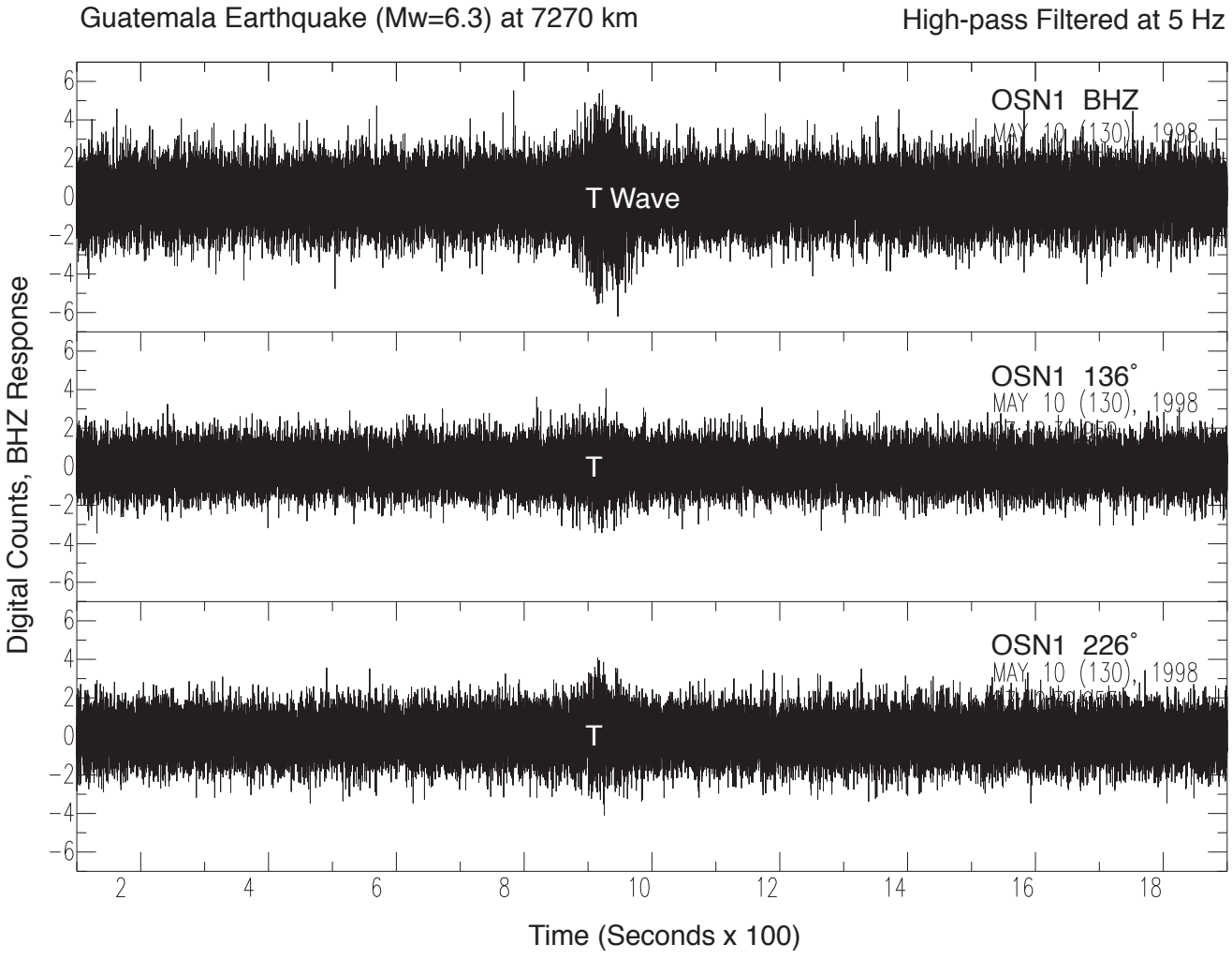
Guatemala Earthquake (Mw=6.3) at 7270 km
High-pass Filtered at 5 Hz
OSN1 BHZ
MAY 10 (130), 1998
T Wave
OSN1 136°
MAY 10 (130), 1998
T
OSN1 226°
MAY 10 (130), 1998
T
Digital Counts, BHZ Response
Time (Seconds x 100)

Figure 8.

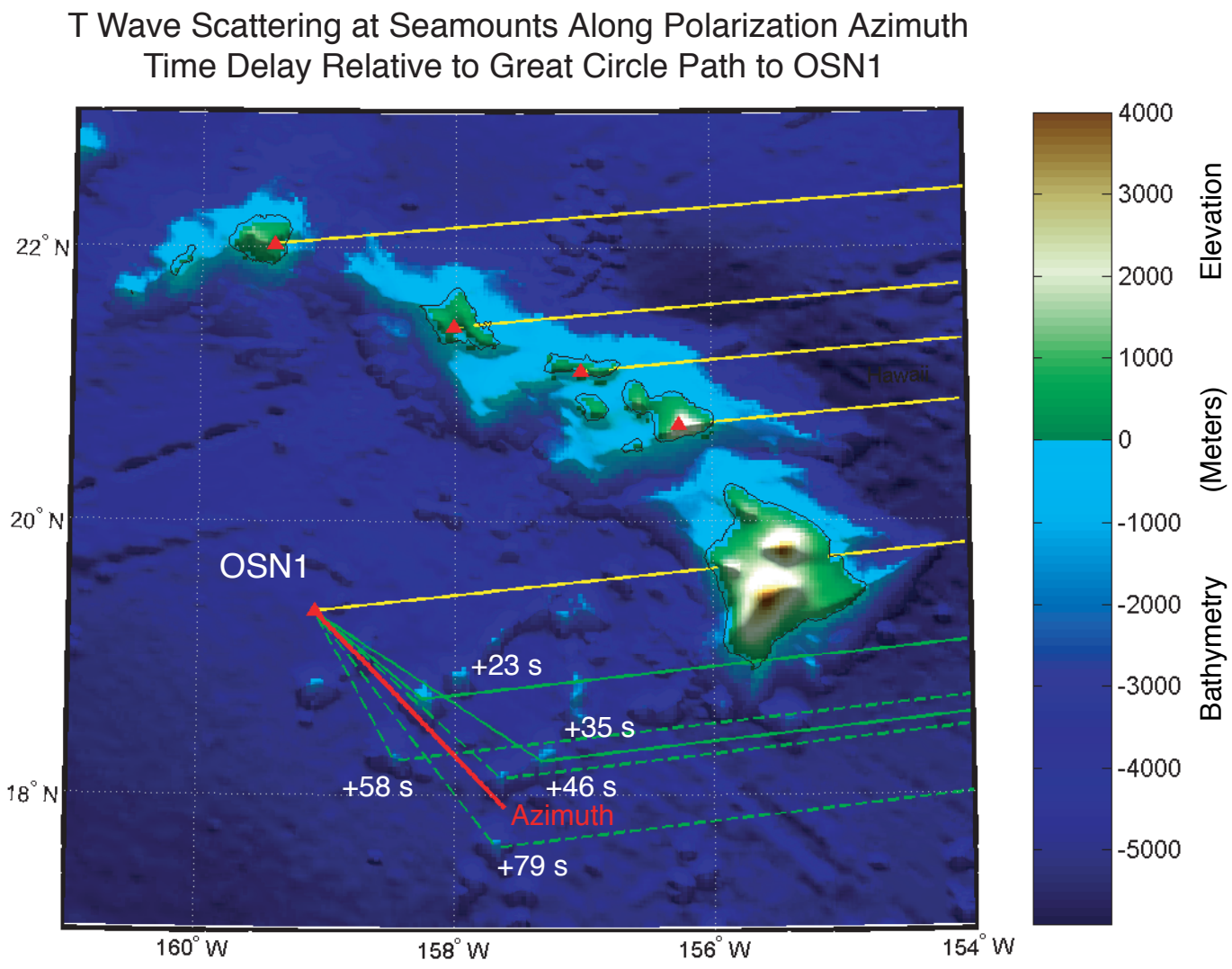
T Wave Scattering at Seamounts Along Polarization Azimuth
Time Delay Relative to Great Circle Path to OSN1
22° N
20° N
18° N
160° W
158° W
156° W
154° W
Hawaii
OSN1
+23 s
+35 s
+46 s
+58 s
+79 s
Azimuth
4000
3000
2000
1000
0
-1000
-2000
-3000
-4000
-5000
Elevation
(Meters)
Bathymetry

Figure 9.

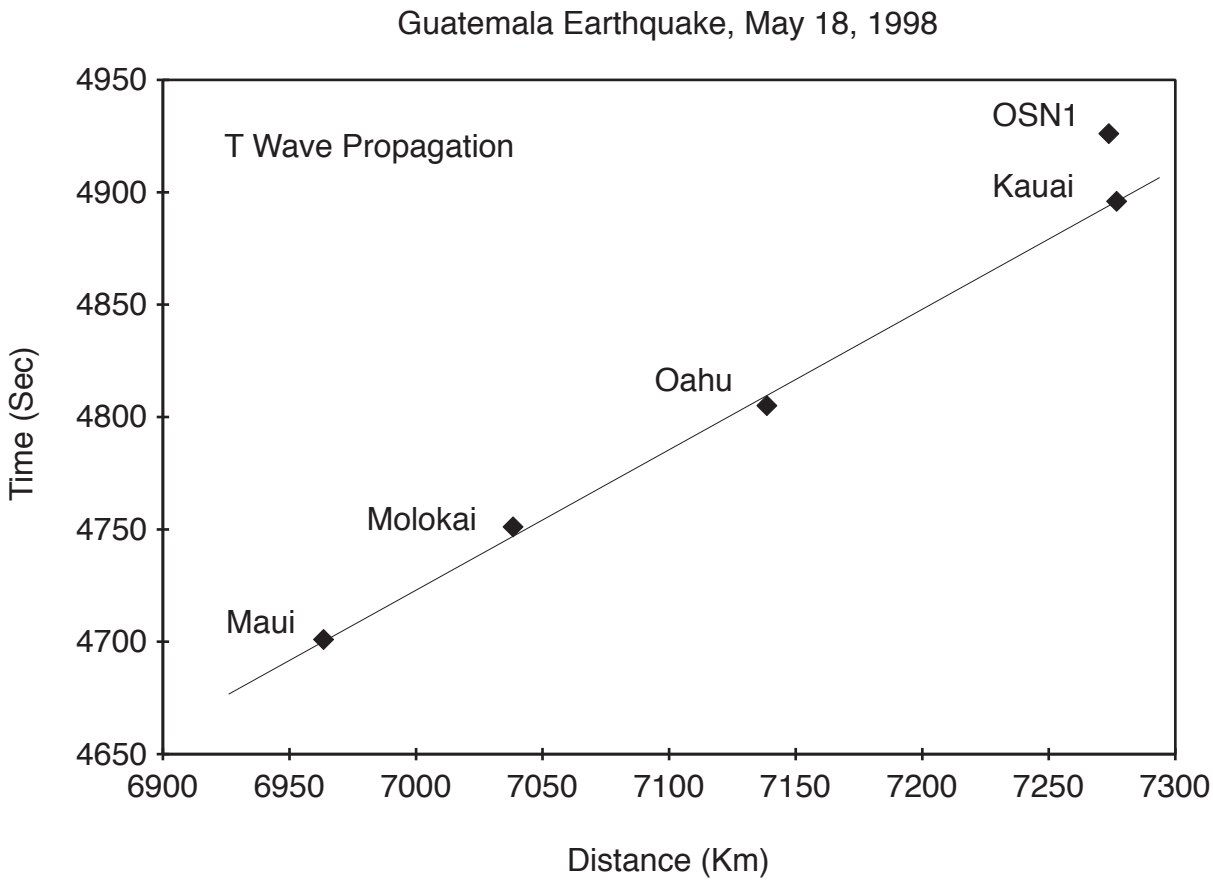
Guatemala Earthquake, May 18, 1998
T Wave Propagation
OSN1
Kauai
Oahu
Molokai
Maui
Time (Sec)
Distance (Km)
4950
4900
4850
4800
4750
4700
4650
6900
6950
7000
7050
7100
7150
7200
7250
7300

Figure 10.

T Wave (>5 Hz) Polarization: Guatemala Earthquake (Mw=6.3) May 10, 1998 at 7270 km

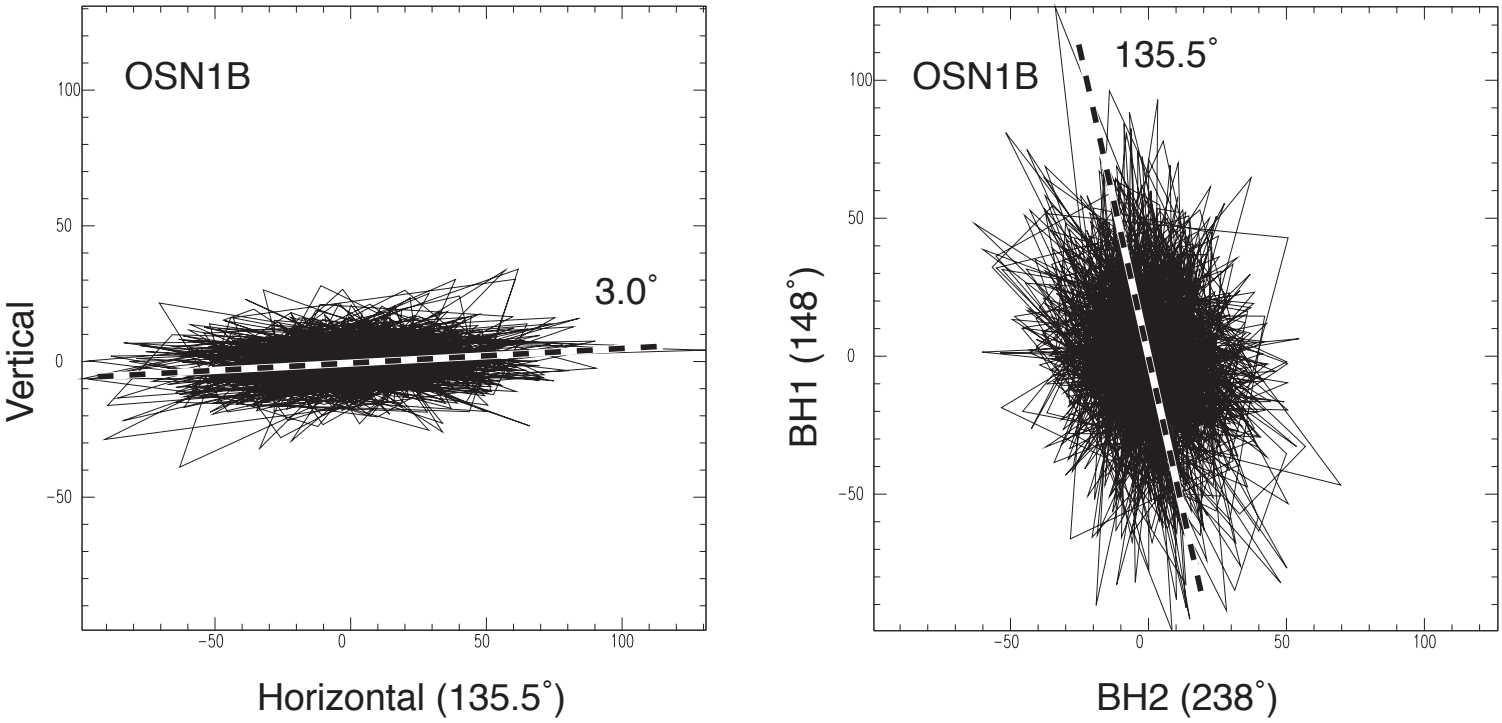

Figure 11.